Supplementary Information

A cyanide-free route towards the electrosynthesis of nitriles

Jiahui Xian[1,2†], Lulu Wang[3†], Ziyu Mi[1,2], Meng Wang[4], Sze Xing Tan[2], Xun Cao[2], Mingsheng Zhang[5], Shibo Xi[2], Jiajian Gao[2], Yanwei Lum[4], Pengfei Ou[3]* and Wan Ru Leow[1,2]*

[1]School of Chemistry, Chemical Engineering and Biotechnology, Nanyang Technological University; 21 Nanyang Link, Nanyang Technological University, Singapore 637371, Republic of Singapore

[2]Institute of Sustainability for Chemicals Energy and Environment (ISCE[2]), Agency for Science, Technology and Research (A*STAR); 1 Pesek Road Jurong Island, Singapore 627833, Republic of Singapore

[3]Department of Chemistry, National University of Singapore, 3 Science Drive 3, Singapore 117543, Republic of Singapore

[4]Department of Chemical and Biomolecular Engineering, National University of Singapore, Singapore 117585, Republic of Singapore

[5]Institute of Materials Research and Engineering (IMRE), Agency for Science, Technology and Research (A*STAR); 2 Fusionopolis Way, #08-03 Innovis, Singapore 138634, Republic of Singapore

*Corresponding authors. Email: wanru.leow@ntu.edu.sg; pengf.ou@nus.edu.sg

†These authors contributed equally to this work.

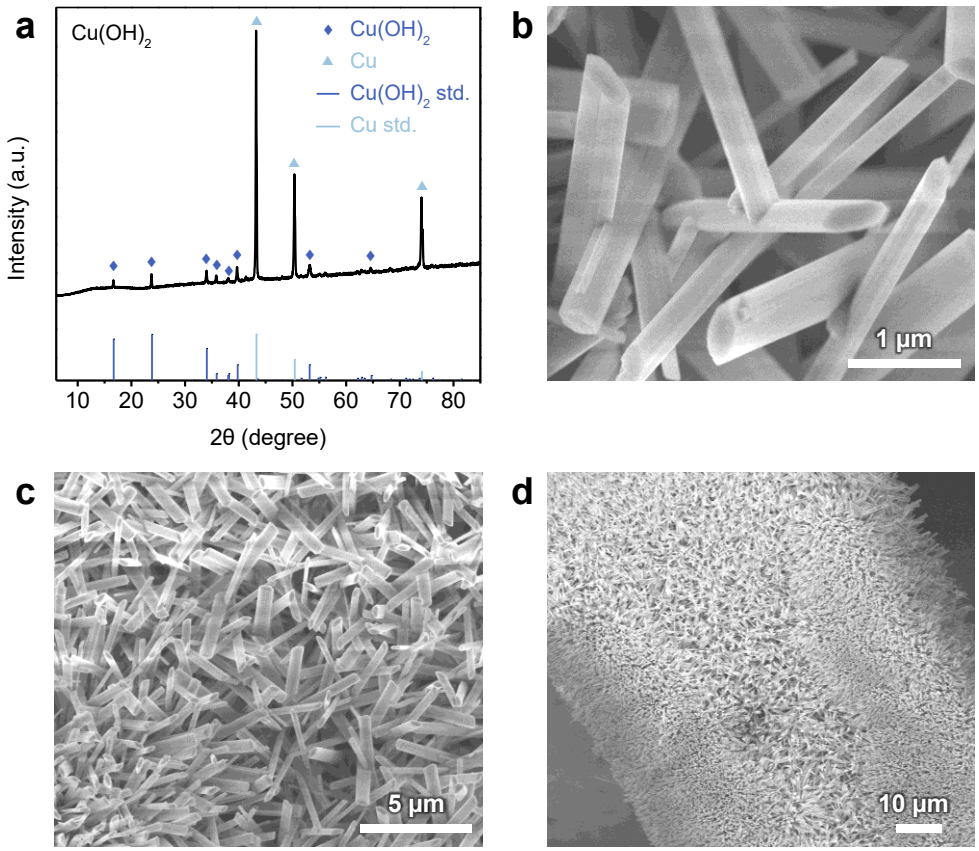

Supplementary Fig. 1 | a, XRD pattern and **b-d**, SEM images of the $Cu(OH)_2$ nanorod array at different magnifications. Source data for Supplementary Fig. 1a are provided as Source Data file.

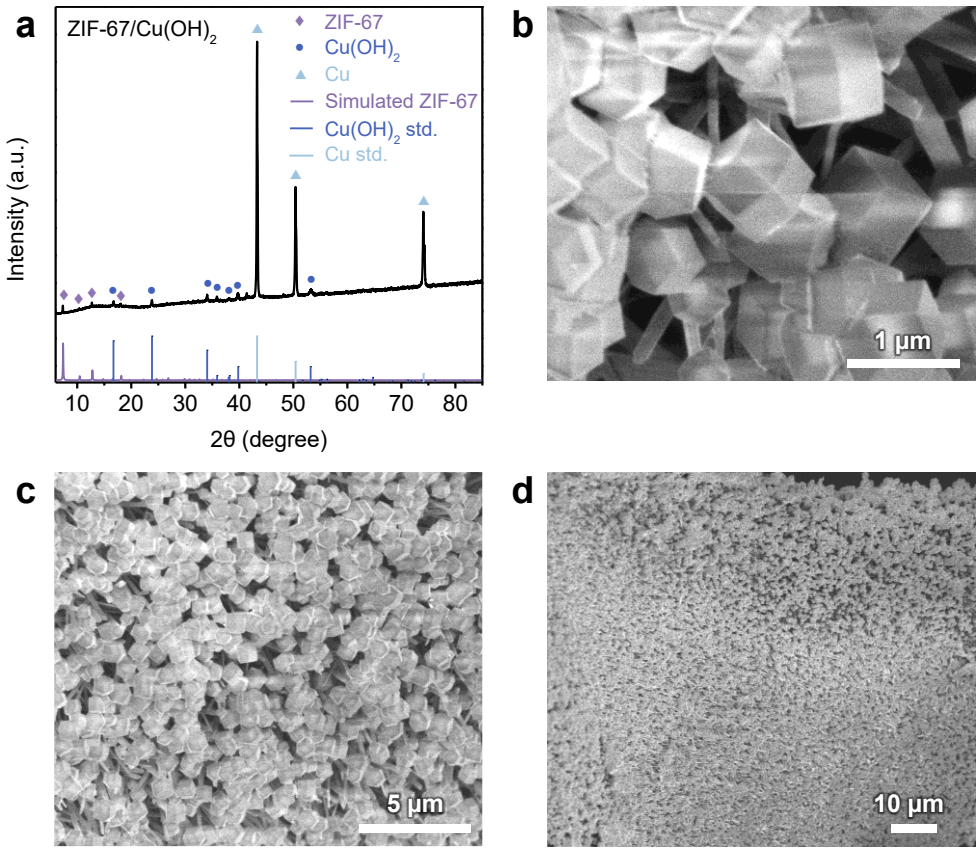

Supplementary Fig. 2 | a, XRD pattern and **b-d**, SEM images of the ZIF-67/$Cu(OH)_2$ nanorod array at different magnifications. Source data for Supplementary Fig. 2a are provided as Source Data file.

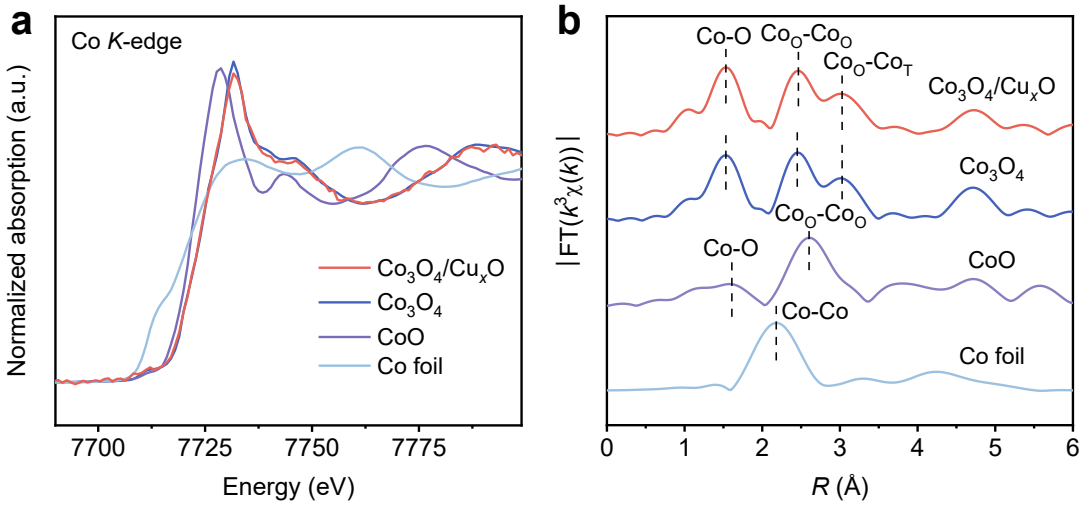

Supplementary Fig. 3 | a, XANES spectra at Co *K*-edge and **b**, Fourier-transformed (FT) k^3-weighted $\chi(k)$-function EXAFS spectra of the Co_3O_4/Cu_xO electrocatalyst versus that of Co_3O_4, CoO and Co foil references. Source data for Supplementary Fig. 3a and 3b are provided as Source Data file.

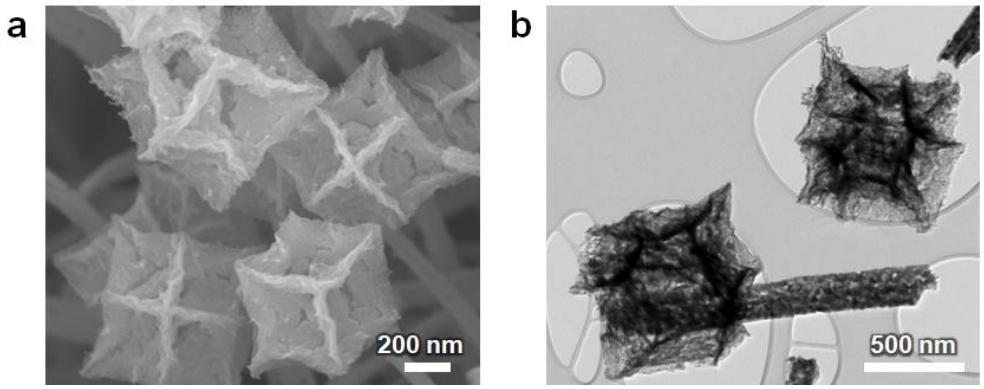

Supplementary Fig. 4 | a, SEM and **b**, TEM images of the Co_3O_4/Cu_xO electrocatalyst.

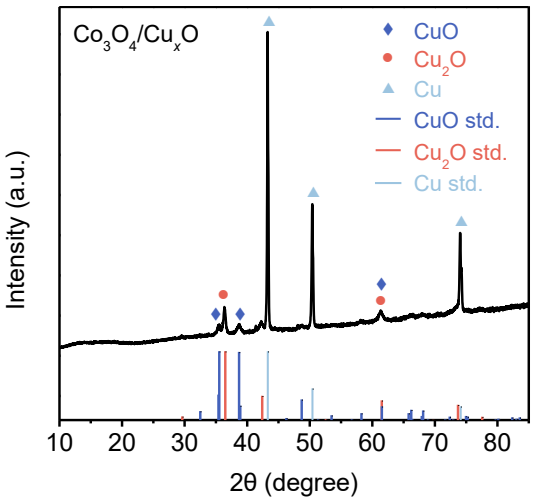

Supplementary Fig. 5 | XRD pattern of the Co_3O_4/Cu_xO electrocatalyst. Source data for Supplementary Fig. 5 are provided as Source Data file.

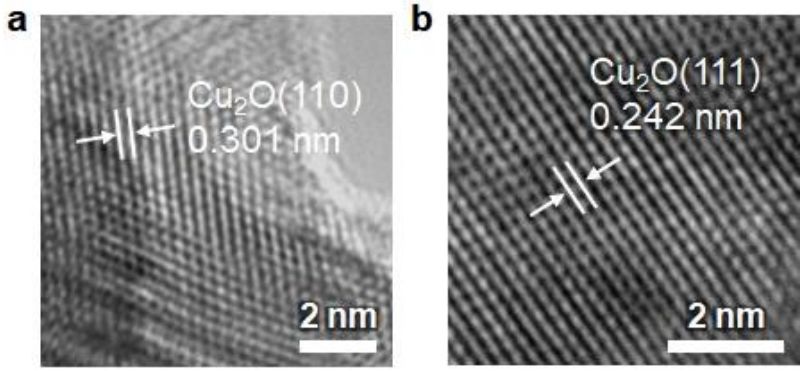

Supplementary Fig. 6 | HRTEM images of the **a,** $Cu_2O(110)$ facet and **b,** $Cu_2O(111)$ facet in the Co_3O_4/Cu_xO electrocatalyst.

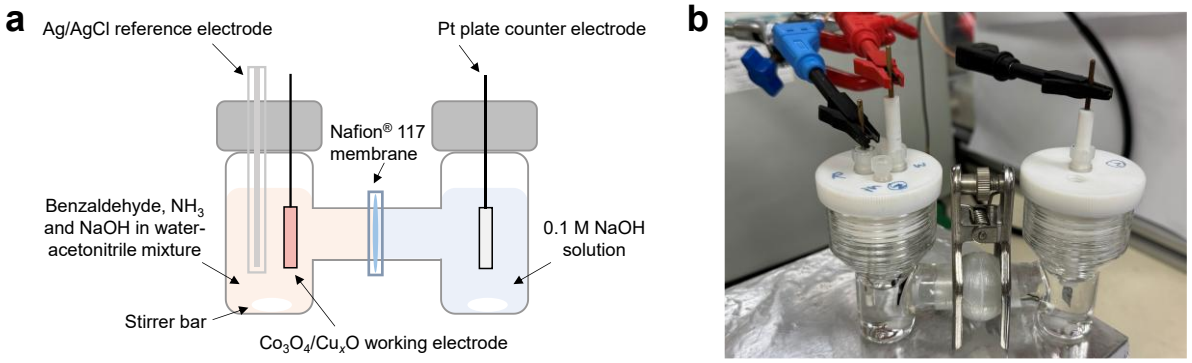

Supplementary Fig. 7 | **a**, Schematic illustration and **b**, photograph of benzonitrile electrosynthesis in an H-type cell configuration. The stirrer bar rotates at 300 rpm.

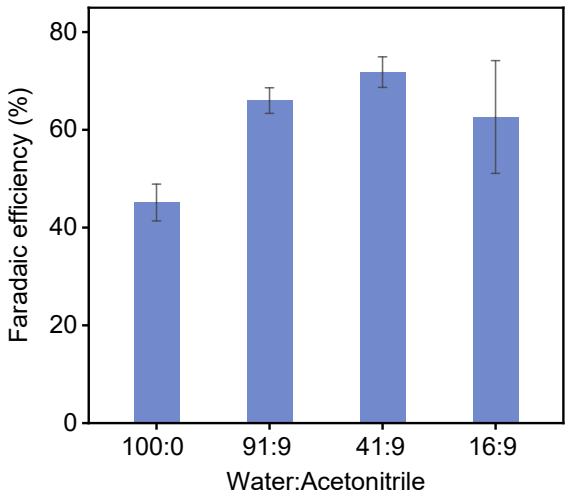

Supplementary Fig. 8 | Faradaic efficiencies of the electrochemical benzaldehyde-to-benzonitrile conversion using electrolytes comprising different water:acetonitrile ratios. The electrocatalyst used is Cu_xO and the potential is 1.35 V vs. RHE. All error bars represent standard deviation based on three independent samples. Source data for Supplementary Fig. 8 and 3b are provided as Source Data file.

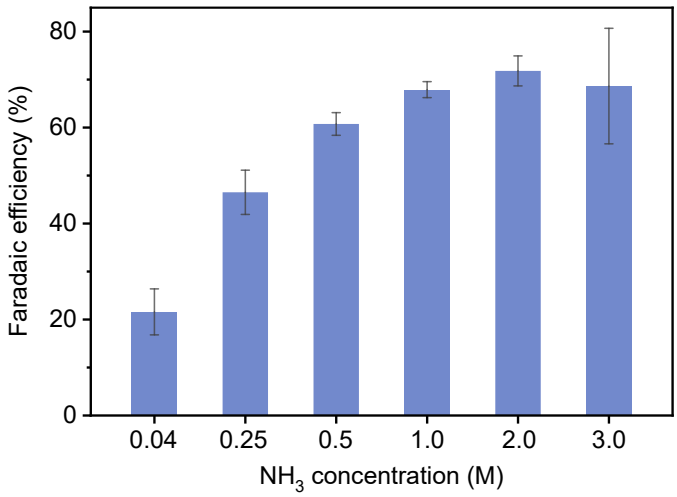

Supplementary Fig. 9 | Faradaic efficiencies of the electrochemical benzaldehyde-to-benzonitrile conversion under various NH_3 concentrations. The electrocatalyst used is Cu_xO and the potential is 1.35 V vs. RHE. All error bars represent standard deviation based on three independent samples. Source data for Supplementary Fig. 9 are provided as Source Data file.

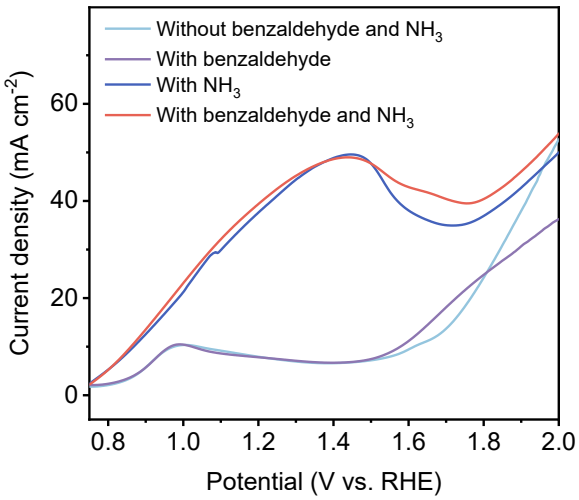

Supplementary Fig. 10 | LSV curves of the Co_3O_4/Cu_xO electrocatalyst under different reaction conditions. All measurements were conducted without iR compensation. Source data for Supplementary Fig. 10 are provided as Source Data file.

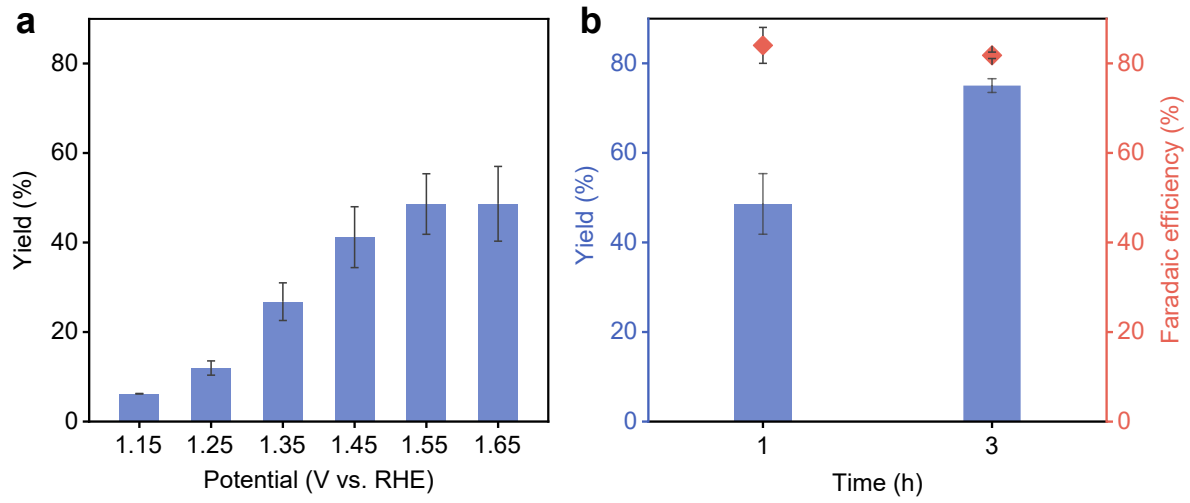

Supplementary Fig. 11 | Benzonitrile yields achieved with the Co_3O_4/Cu_xO electrocatalyst at **a,** potentials 1.15-1.65 V vs RHE and **b,** 1 versus 3 hours at 1.55 V vs. RHE. All measurements were conducted without iR compensation. All error bars represent standard deviation based on three independent samples. Source data for Supplementary Fig. 11a and 11b are provided as Source Data file.

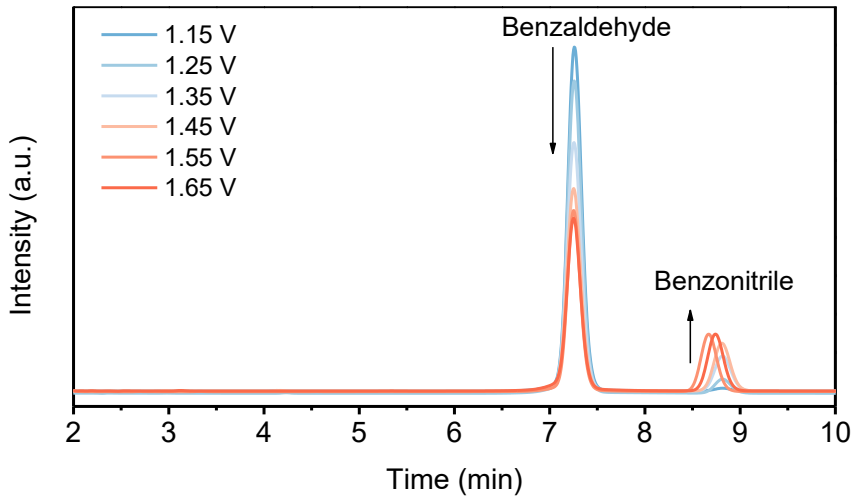

Supplementary Fig. 12 | The HPLC chromatograms of the anolyte after reaction with the Co_3O_4/Cu_xO electrocatalyst at different potentials. Source data for Supplementary Fig. 12 are provided as Source Data file.

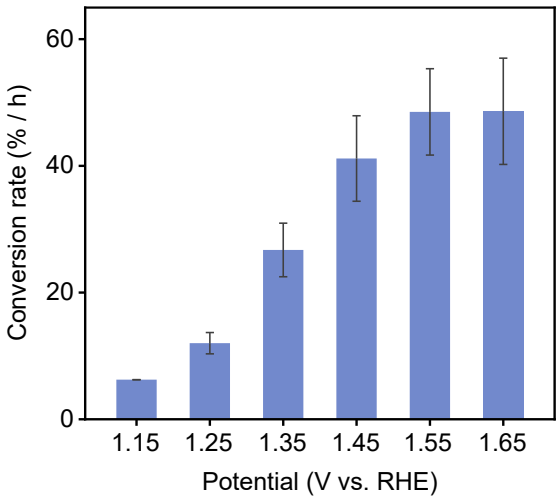

Supplementary Fig. 13 | Benzaldehyde conversion rates achieved with the Co_3O_4/Cu_xO electrocatalyst at 1.15-1.65 V vs. RHE. All error bars represent standard deviation based on three independent samples. Source data for Supplementary Fig. 13 are provided as Source Data file.

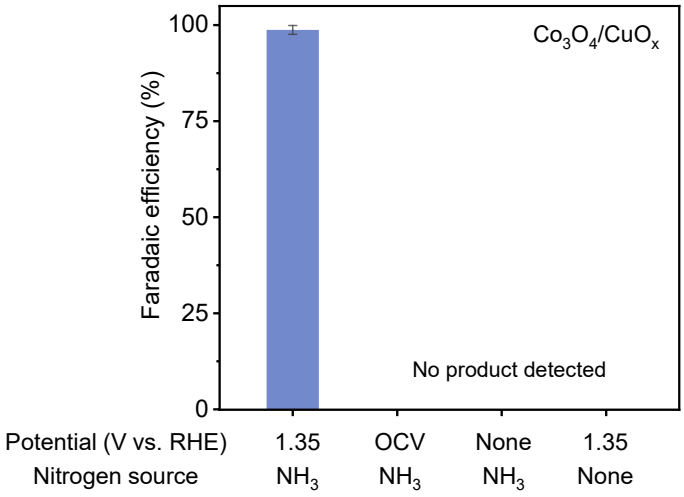

Supplementary Fig. 14 | Faradaic efficiencies of the electrochemical benzaldehyde-to-benzonitrile conversion using Co_3O_4/Cu_xO electrocatalyst at different reaction conditions. All measurements were conducted without iR compensation. All error bars represent standard deviation based on three independent samples. Source data for Supplementary Fig. 14 are provided as Source Data file.

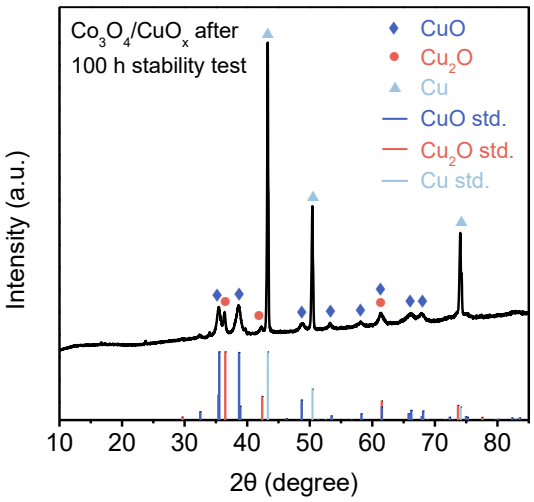

Supplementary Fig. 15 | XRD pattern of the Co_3O_4/Cu_xO electrocatalyst after 100 h long-term stability test. Source data for Supplementary Fig. 15 are provided as Source Data file.

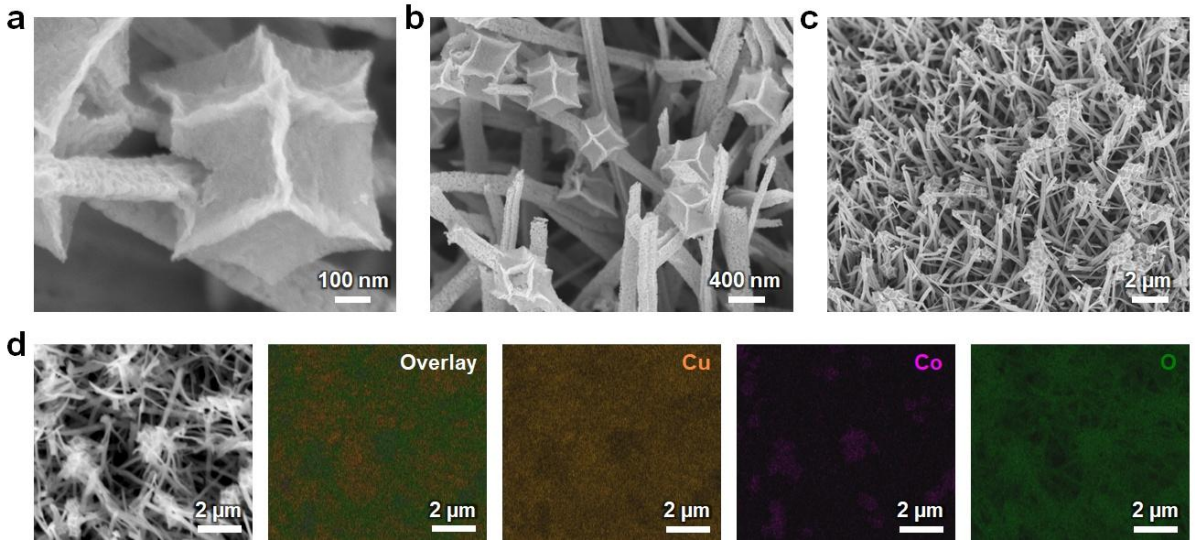

Supplementary Fig. 16 | a-c, SEM images at different magnifications and **d**, SEM-EDX elemental mapping of the Co_3O_4/Cu_xO electrocatalyst after 100 h long-term stability test.

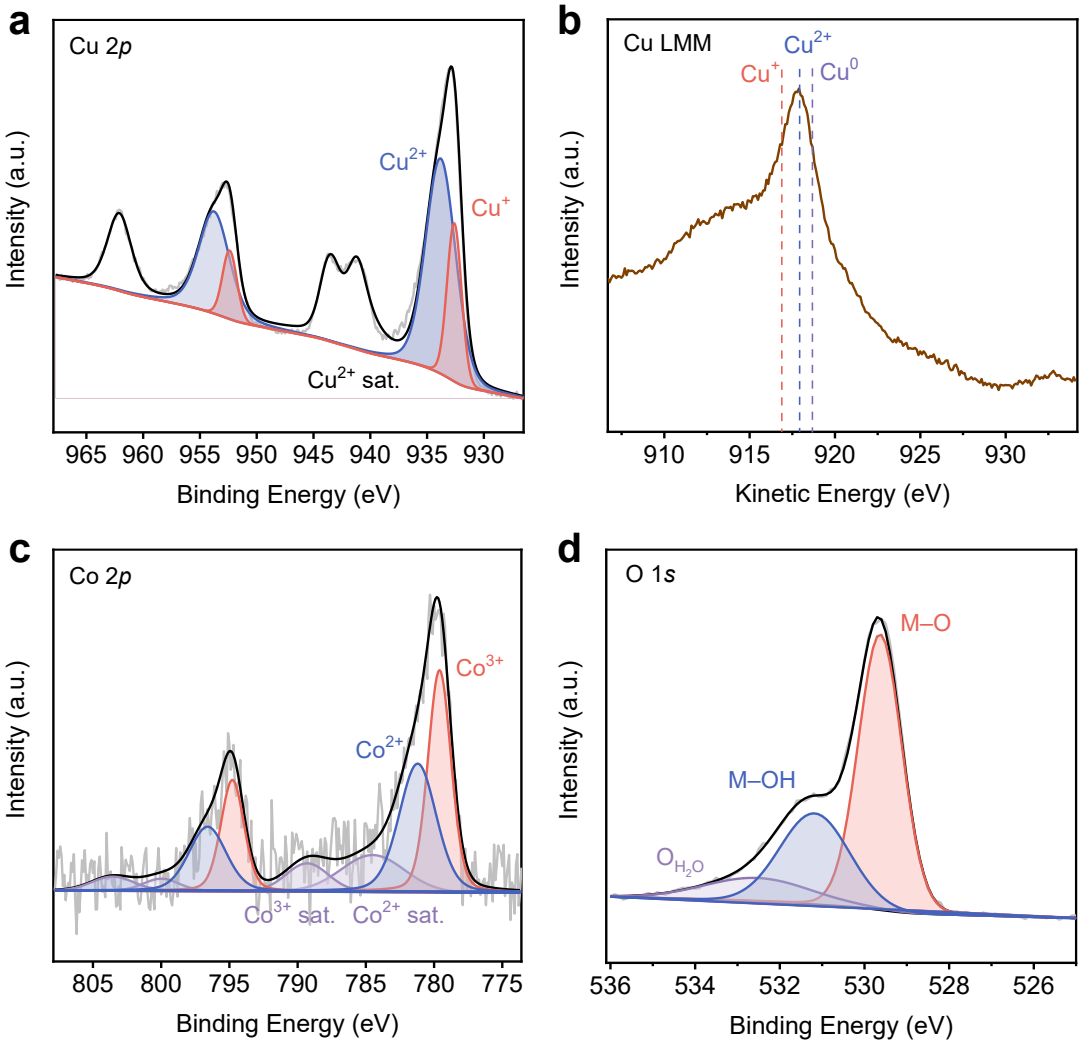

Supplementary Fig. 17 | High-resolution **a**, Cu 2*p*, **b**, Cu LMM Auger electron, **c**, Co 2*p* and **d**, O 1*s* XPS spectra of the Co_3O_4/Cu_xO electrocatalyst after 100 h long-term stability test. Source data for Supplementary Fig. 17a-17d are provided as Source Data file.

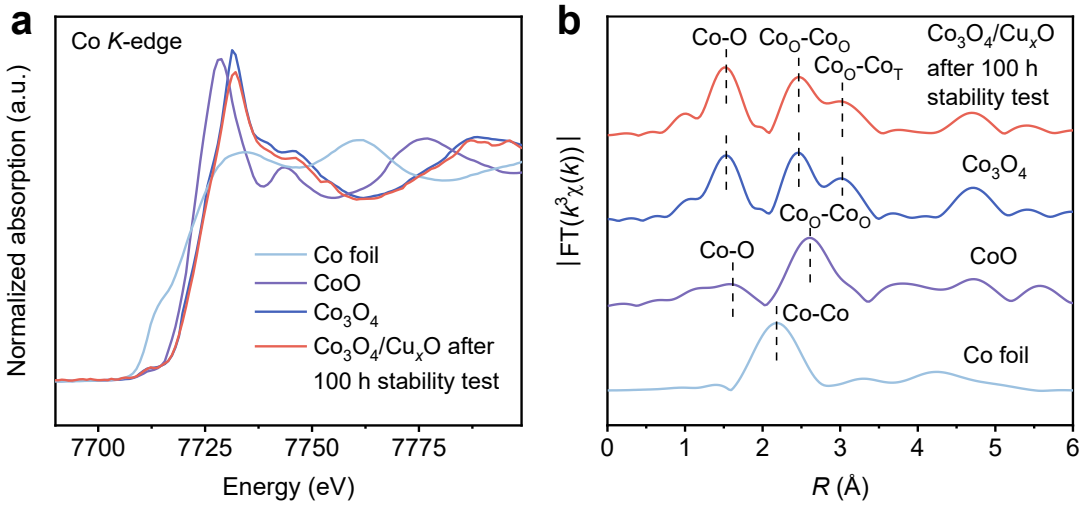

Supplementary Fig. 18 | a, XANES spectra and **b,** Fourier-transformed (FT) k^3-weighted $\chi(k)$-function EXAFS spectra at Co *K*-edge of the Co_3O_4/Cu_xO electrocatalyst after 100 h long-term stability test. Source data for Supplementary Fig. 18a and 18b are provided as Source Data file.

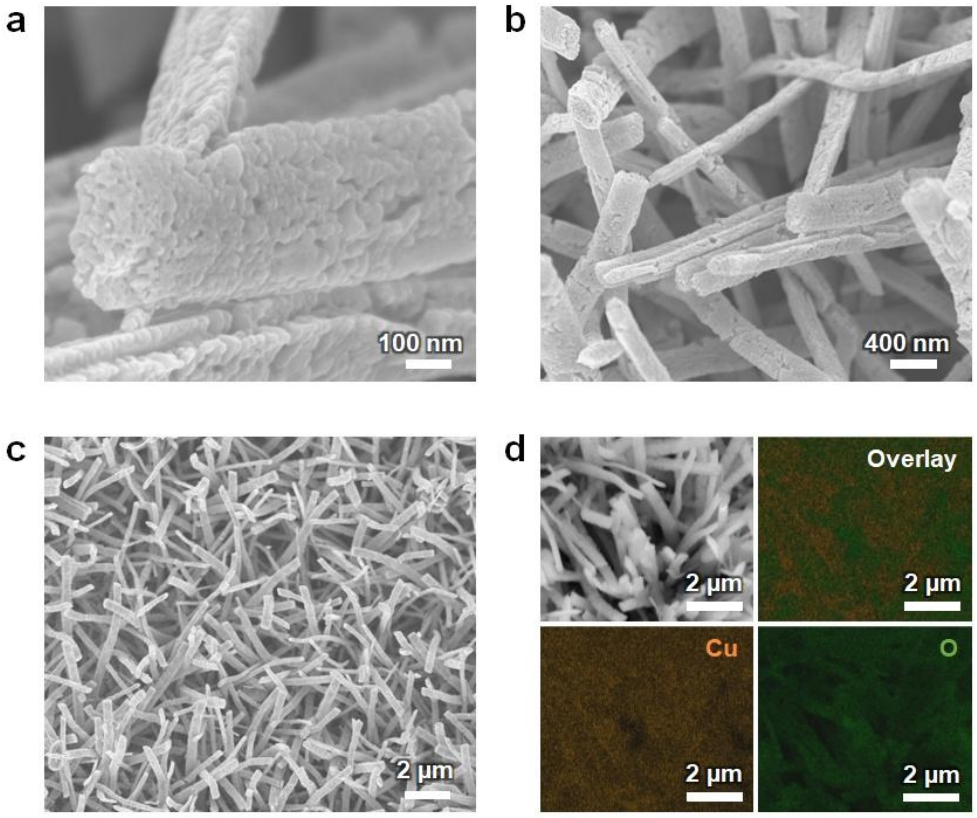

Supplementary Fig. 19 | Morphology characterizations. a-c, SEM images and **d**, SEM-EDX elemental mapping of the Cu_xO electrocatalyst.

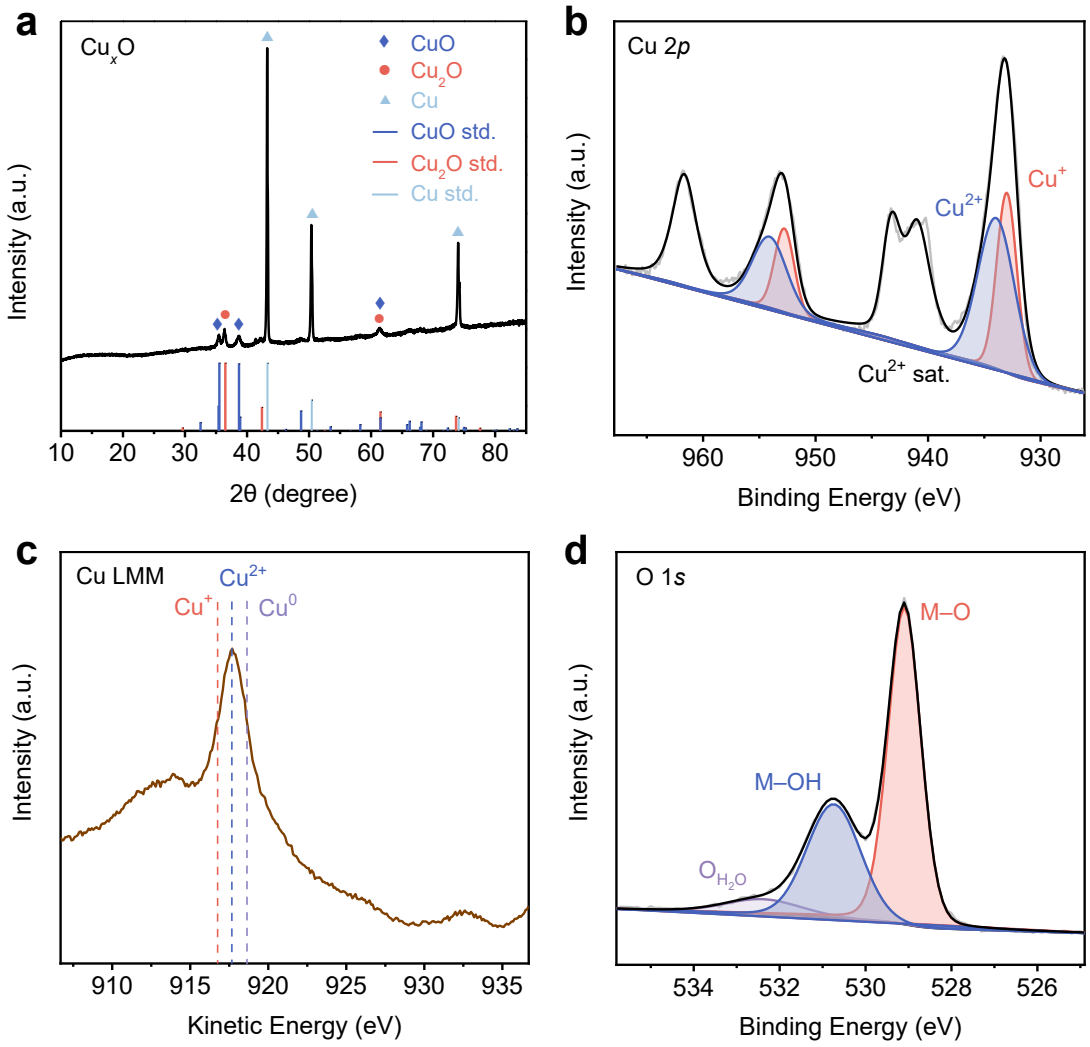

Supplementary Fig. 20 | a, XRD pattern and high-resolution **b**, Cu 2*p*, **c**, Cu LMM Auger electron and **d**, O 1*s* XPS spectra of the Cu_xO electrocatalyst. Source data for Supplementary Fig. 20a-20d are provided as Source Data file.

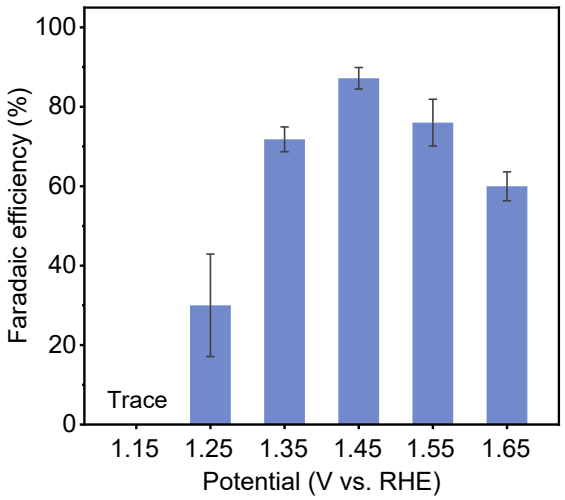

Supplementary Fig. 21 | Faradaic efficiencies of the electrochemical benzaldehyde-to-benzonitrile conversion with the Cu_xO electrocatalyst at different potentials. All measurements were conducted without iR compensation. All error bars represent standard deviation based on three independent samples. Source data for Supplementary Fig. 21 are provided as Source Data file.

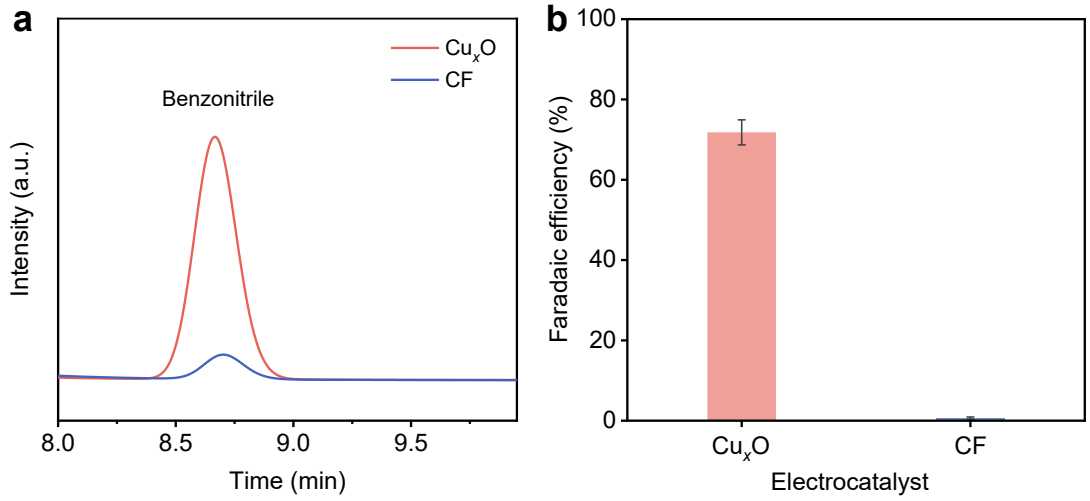

Supplementary Fig. 22 | a, HPLC chromatograms of the post-reaction anolyte and **b**, the corresponding Faradaic efficiency towards benzonitrile after reaction with the Cu_xO and bare copper foam (CF) electrocatalysts at 1.35 V vs. RHE. All error bars represent standard deviation based on three independent samples. Source data for Supplementary Fig. 22a and 22b are provided as Source Data file.

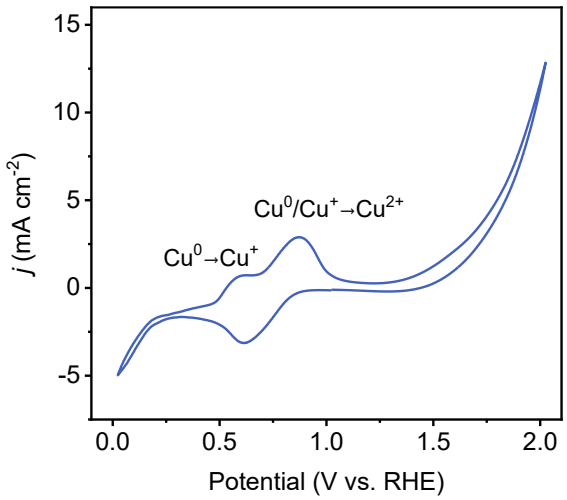

Supplementary Fig. 23 | CV curve of the Cu_xO electrocatalyst in 0.1 M NaOH electrolyte containing benzaldehyde and NH_3 at a scan rate of 5 mV s^{-1}. All measurements were conducted without iR compensation. Source data for Supplementary Fig. 23 are provided as Source Data file.

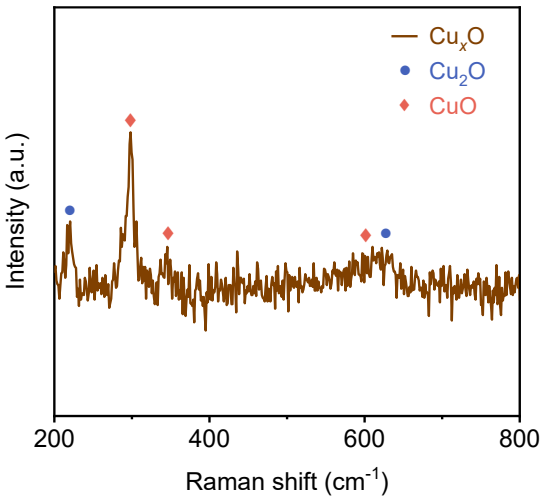

Supplementary Fig. 24 | Raman spectrum of the Cu_xO electrocatalyst. Source data for Supplementary Fig. 24 are provided as Source Data file.

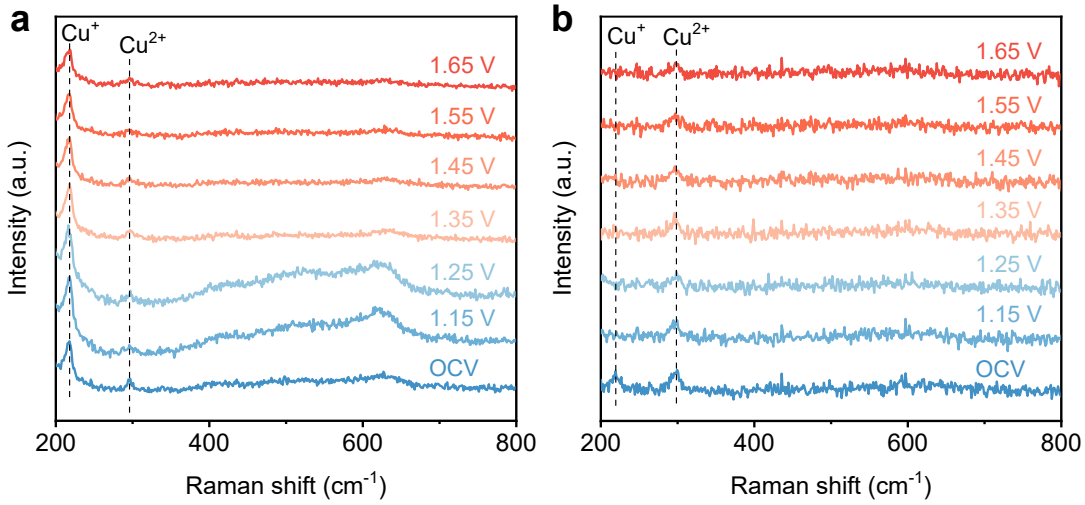

Supplementary Fig. 25 | Potential-dependent in situ Raman spectra of the Cu_xO electrocatalyst in 0.1 M aqueous NaOH electrolyte **a**, with and **b**, without benzaldehyde and NH_3. All measurements were conducted without iR compensation. Source data for Supplementary Fig. 25a and 25b are provided as Source Data file.

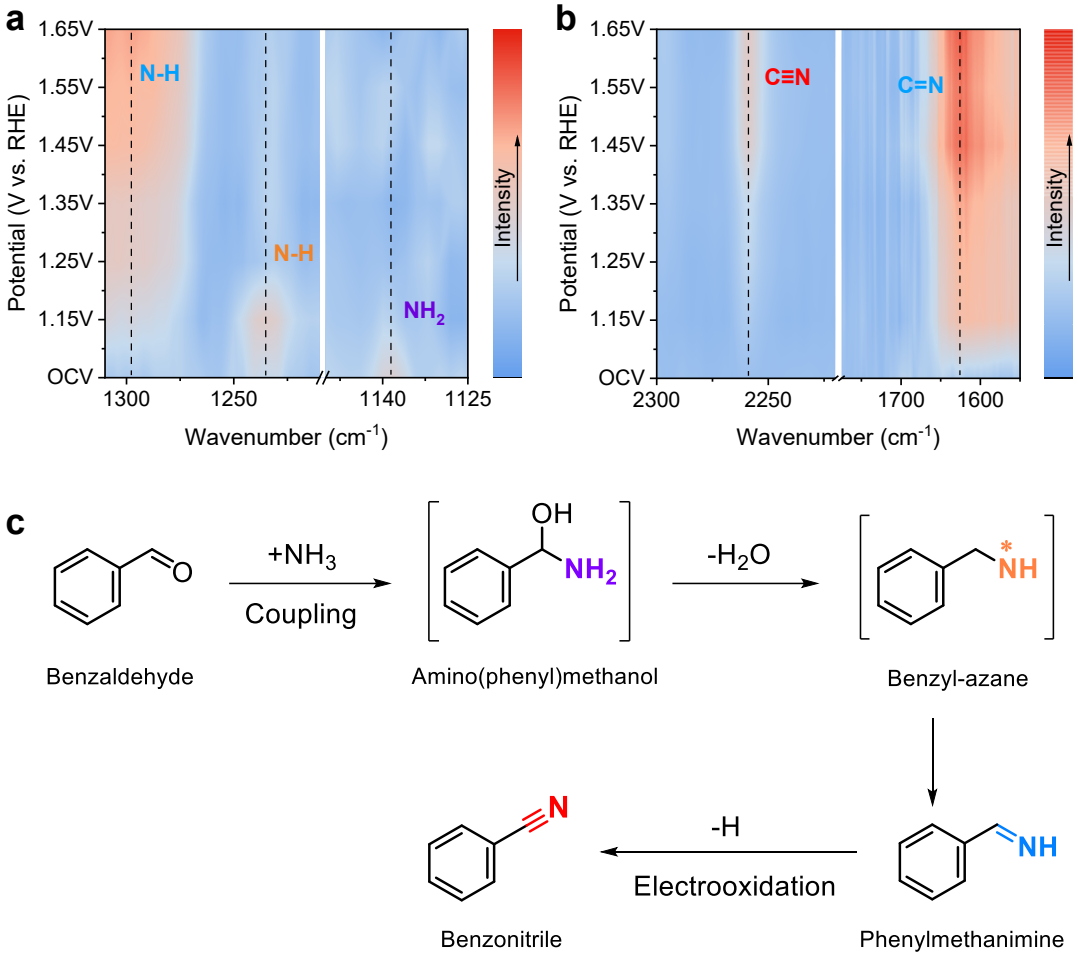

Supplementary Fig. 26 | a-b, Potential-dependent in situ ATR-SEIRAS measurements during the benzonitrile electrosynthesis process. **c**, Detailed illustration of benzonitrile generation pathway. All measurements were conducted without iR compensation. Source data for Supplementary Fig. 26a and 26b are provided as Source Data file.

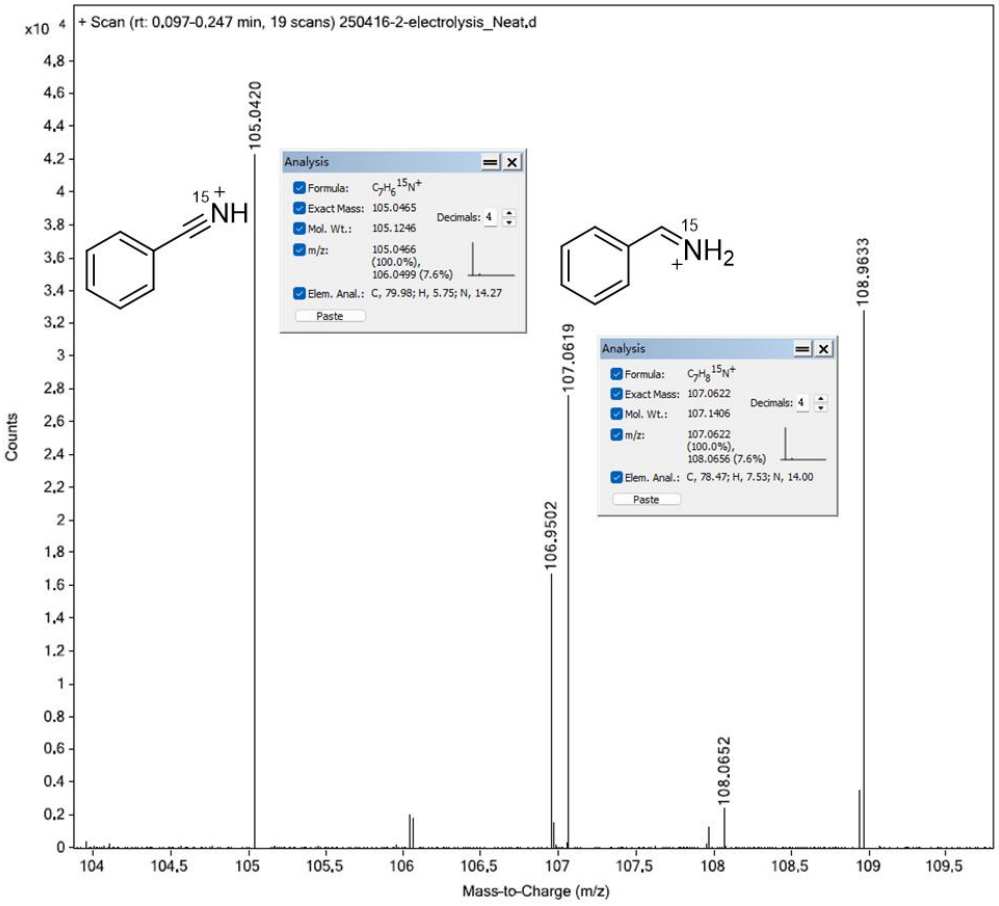

Supplementary Fig. 27 | LC-QTOF spectrum of the ^{15}N-labelled phenylmethanimine intermediate and ^{15}N-labelled benzonitrile in the electrolyte after reaction using benzaldehyde and ^{15}N-labelled NH_3 in H_2O/MeCN solution. The inset shows the molecular formula and the corresponding mass-to-charge analysis. Source data for Supplementary Fig. 27 are provided as Source Data file.

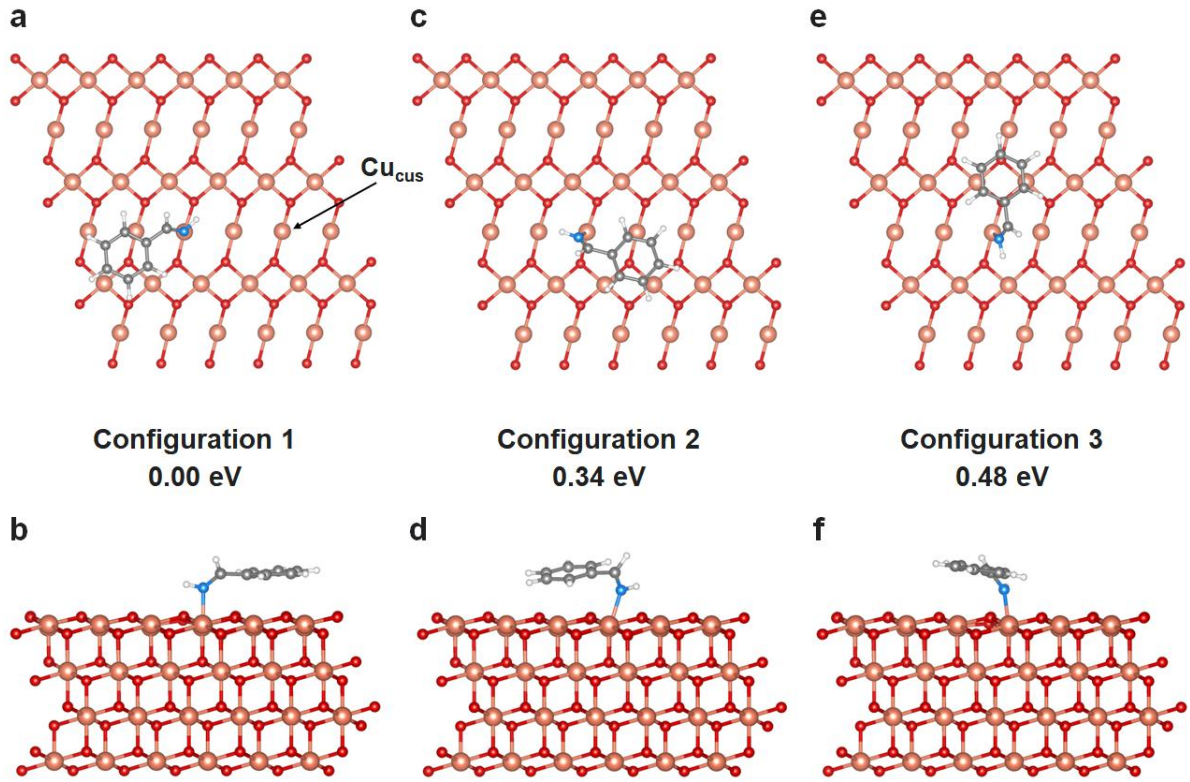

Supplementary Fig. 28 | **a**, **c**, **e**, Top and **b**, **d**, **f**, side views of phenylmethanimine (*Ph−CH=NH) adsorbed in three distinct configurations on the CuO(111) surface. In all cases, the molecule is anchored at the coordinatively unsaturated Cu (Cu_{cus}) site. The relative energies of all configurations are labeled, using Configuration 1 as the zero-energy baseline (0.00 eV). Cu, O, N, C and H atoms are depicted here as orange, red, blue, gray and white spheres, respectively. Source data for Supplementary Fig. 28 are provided as Source Data file.

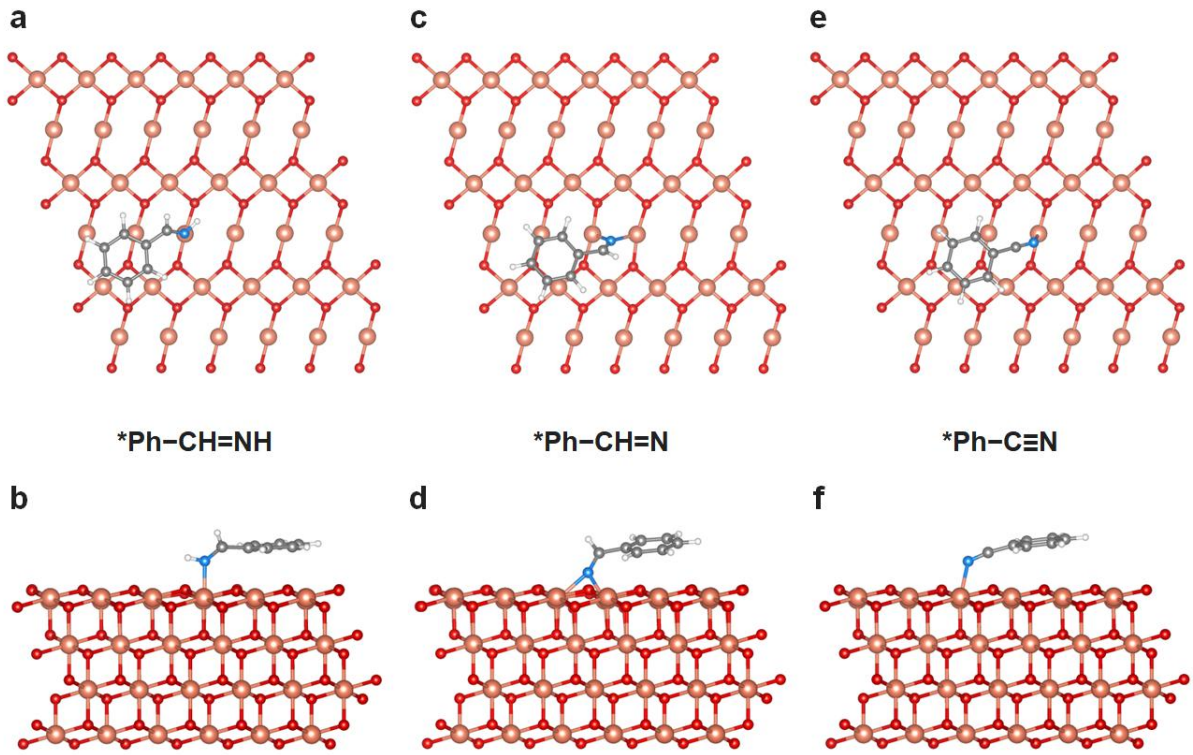

Supplementary Fig. 29 | The optimized structures of *Ph−CH=NH (**a**, top view and **b**, side view), *Ph−CH=N (**c**, top view and **d**, side view) and *Ph−C≡N (**e**, top view and **f**, side view) absorbed on the CuO(111) surface. Cu, O, N, C and H atoms are depicted here as orange, red, blue, gray and white spheres, respectively.

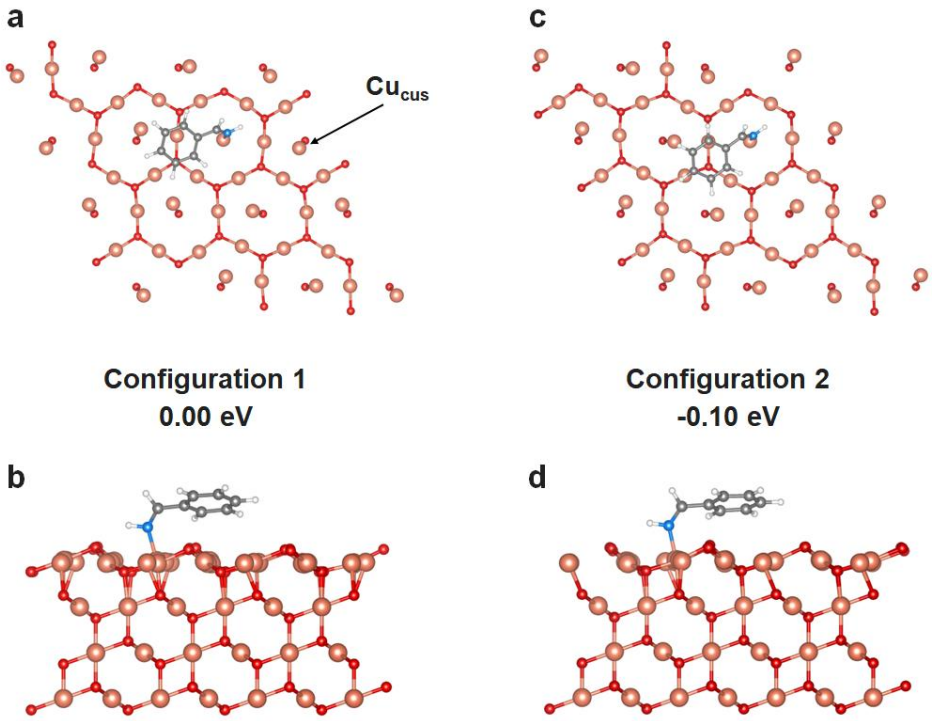

Supplementary Fig. 30 | **a**, **c**, Top and **b**, **d**, side views of phenylmethanimine (*Ph−CH=NH) adsorbed in two distinct configurations on the $Cu_2O(111)$ surface. In all cases, the molecule is anchored at the coordinatively unsaturated Cu (Cu_{cus}) site. The relative energies of all configurations are labeled, using Configuration 1 as the zero-energy baseline (0.00 eV). Cu, O, N, C and H atoms are depicted here as orange, red, blue, gray and white spheres, respectively. Source data for Supplementary Fig. 30 are provided as Source Data file.

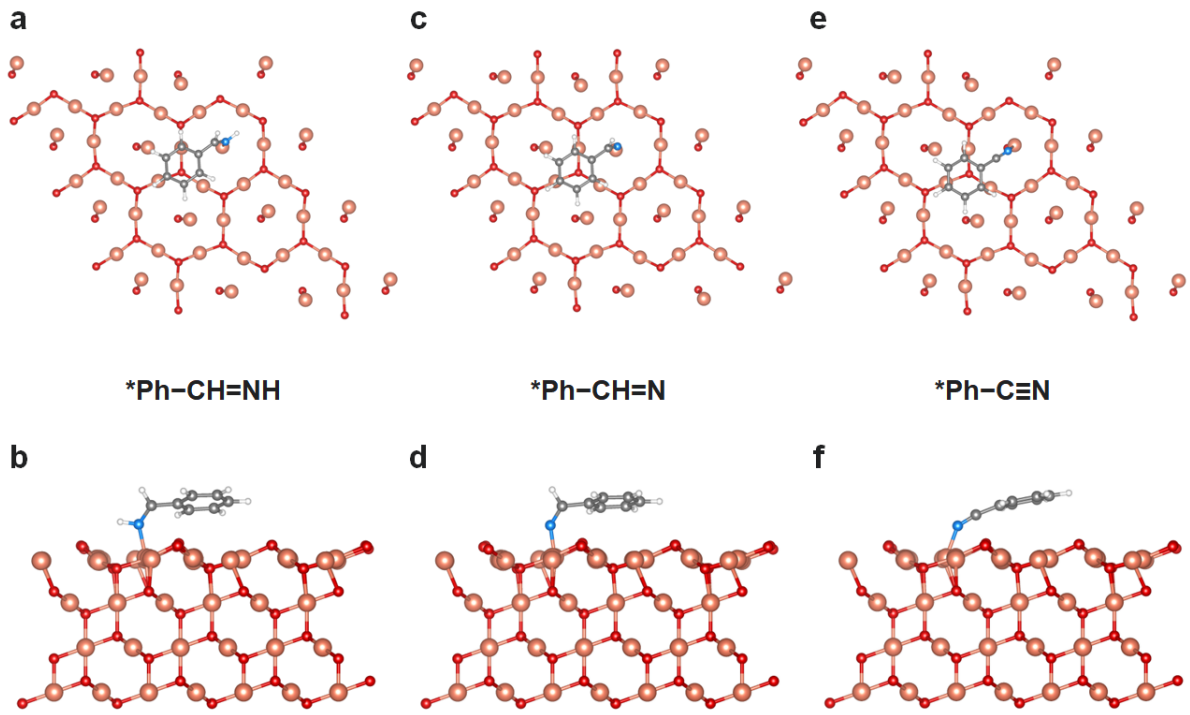

Supplementary Fig. 31 | The optimized structures of *Ph−CH=NH (**a**, top view and **b**, side view), *Ph−CH=N (**c**, top view and **d**, side view) and *Ph−C≡N (**e**, top view and **f**, side view) absorbed on the $Cu_2O(111)$ surface. Cu, O, N, C and H atoms are depicted here as orange, red, blue, gray and white spheres, respectively.

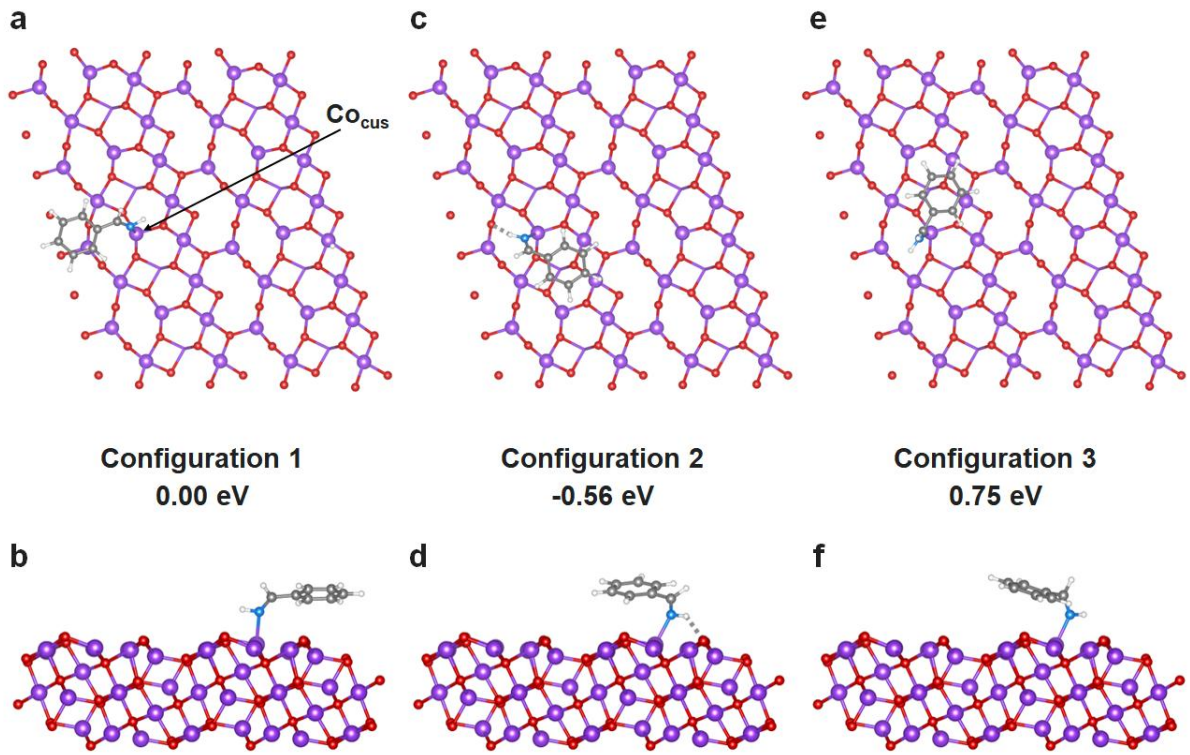

Supplementary Fig. 32 | **a**, **c**, **e**, Top and **b**, **d**, **f**, side views of phenylmethanimine (*Ph−CH=NH) adsorbed in three distinct configurations on the Co_3O_4(311) surface. In all cases, the molecule is anchored at the coordinatively unsaturated Co (Cu_{cus}) site. The relative energies of all configurations are labeled, using Configuration 1 as the zero-energy baseline (0.00 eV). Co, O, N, C and H atoms are depicted here as purple, red, blue, gray and white spheres, respectively. Source data for Supplementary Fig. 32 are provided as Source Data file.

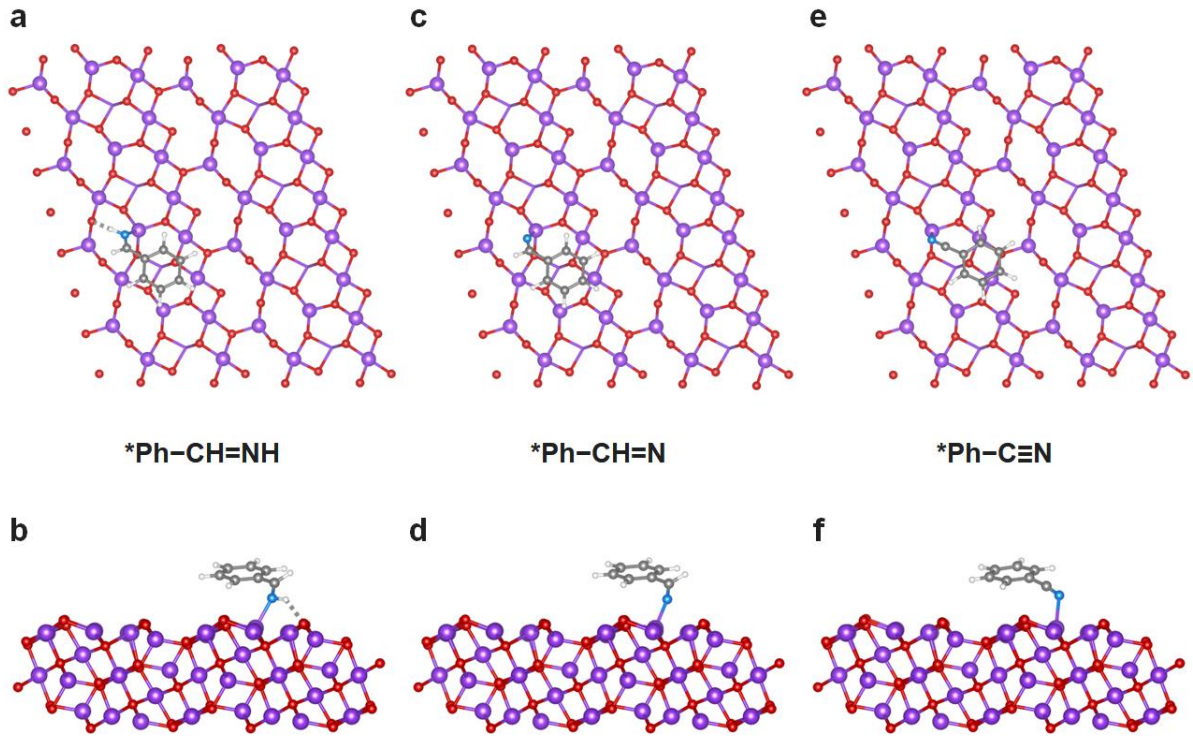

Supplementary Fig. 33 | The optimized structures of *Ph−CH=NH (**a**, top view and **b**, side view), *Ph−CH=N (**c**, top view and **d**, side view) and *Ph−C≡N (**e**, top view and **f**, side view) absorbed on the Co_3O_4(311) surface. Co, O, N, C and H atoms are depicted here as purple, red, blue, gray and white spheres, respectively.

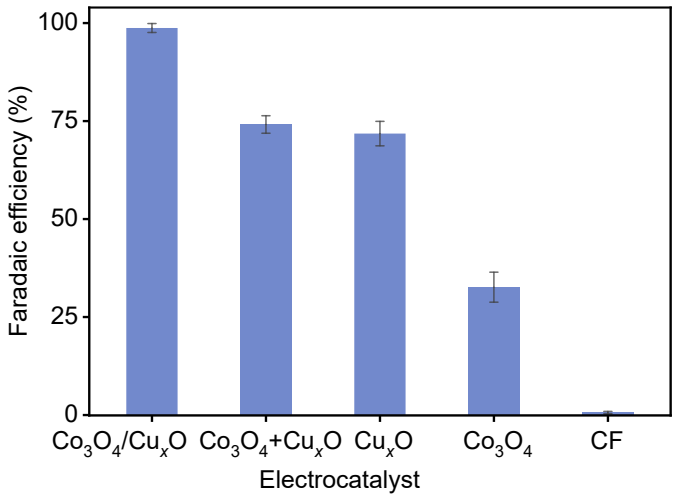

Supplementary Fig. 34 | The Faradaic efficiency of benzonitrile on different electrocatalysts at 1.35 V vs. RHE. All error bars represent standard deviation based on three independent samples. Source data for Supplementary Fig. 34 are provided as Source Data file.

Note: Co_3O_4+Cu_xO refers to a physically mixed catalyst without the contact edge, prepared by drop-casting the Co_3O_4 ink onto the Cu_xO electrode. The Faradaic efficiency of Co_3O_4+Cu_xO is inferior to that of the Co_3O_4/Cu_xO electrocatalyst, and comparable to that of Cu_xO electrocatalyst. This indicates that the interfacial interaction is critical, and is consistent with our observation that the Co_3O_4/Cu_xO contact edge results in a higher average Cu oxidation state, which promotes the $Cu^{\delta+}$-mediated dehydrogenation step and enables increased Faradaic efficiency.

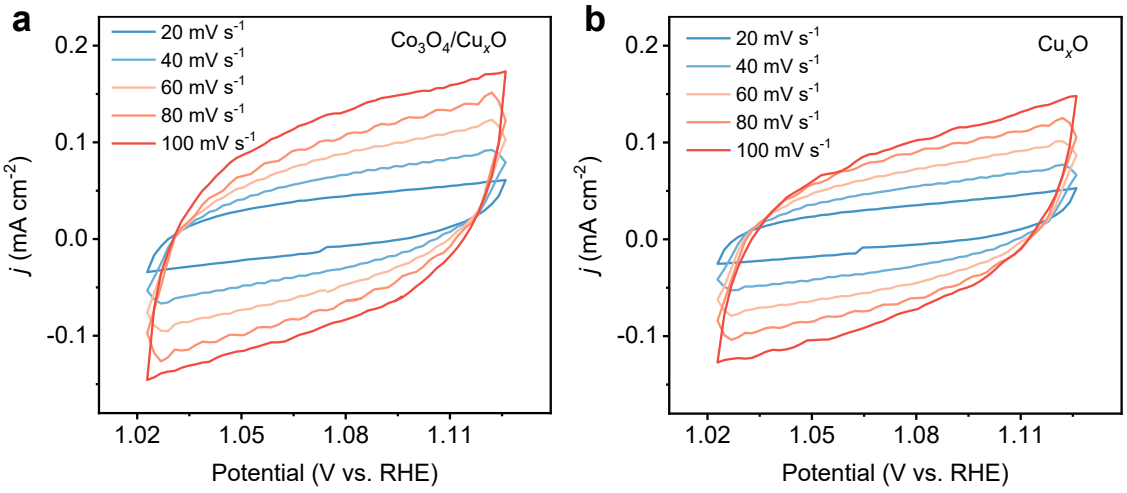

Supplementary Fig. 35 | CV curves in a non-Faradaic region at different scan rates with the **a**, Co_3O_4/Cu_xO and **b**, Cu_xO electrocatalysts. All measurements were conducted without iR compensation. Source data for Supplementary Fig. 35a and 35b are provided as Source Data file.

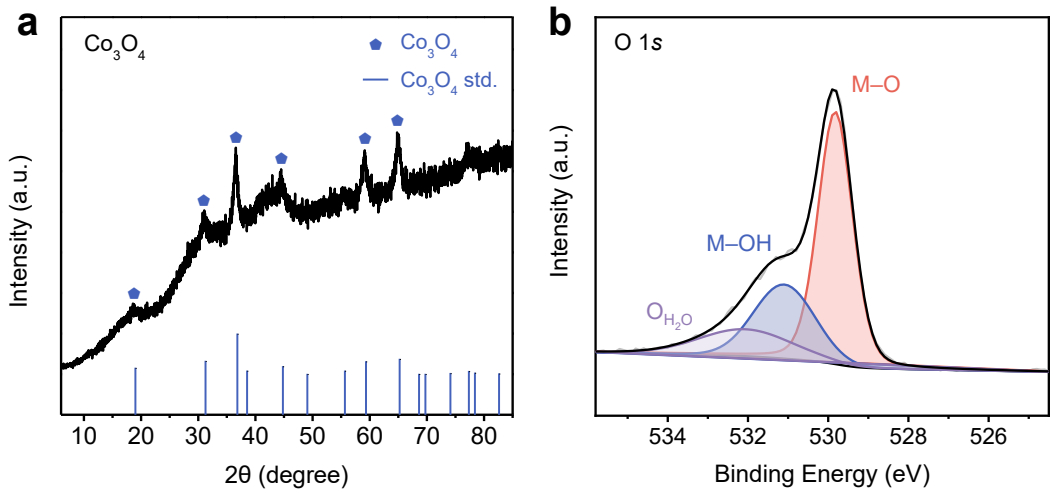

Supplementary Fig. 36 | a, XRD pattern and **b**, O 1*s* XPS spectrum of the synthesized Co_3O_4 powder. Source data for Supplementary Fig. 36a and 36b are provided as Source Data file.

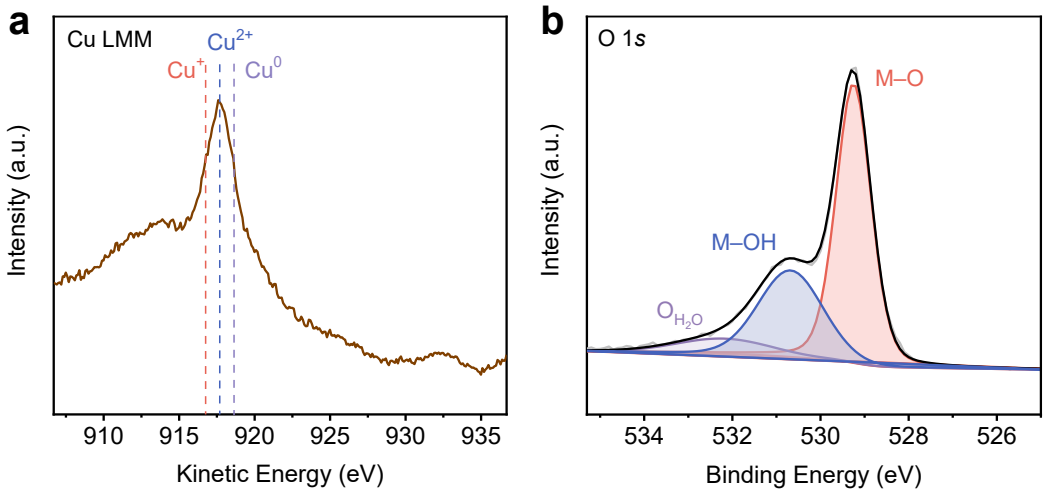

Supplementary Fig. 37 | High-resolution **a**, Cu LMM Auger electron spectrum and **b**, O 1*s* XPS spectrum of the Co_3O_4/Cu_xO electrocatalyst. Source data for Supplementary Fig. 37a and 37b are provided as Source Data file.

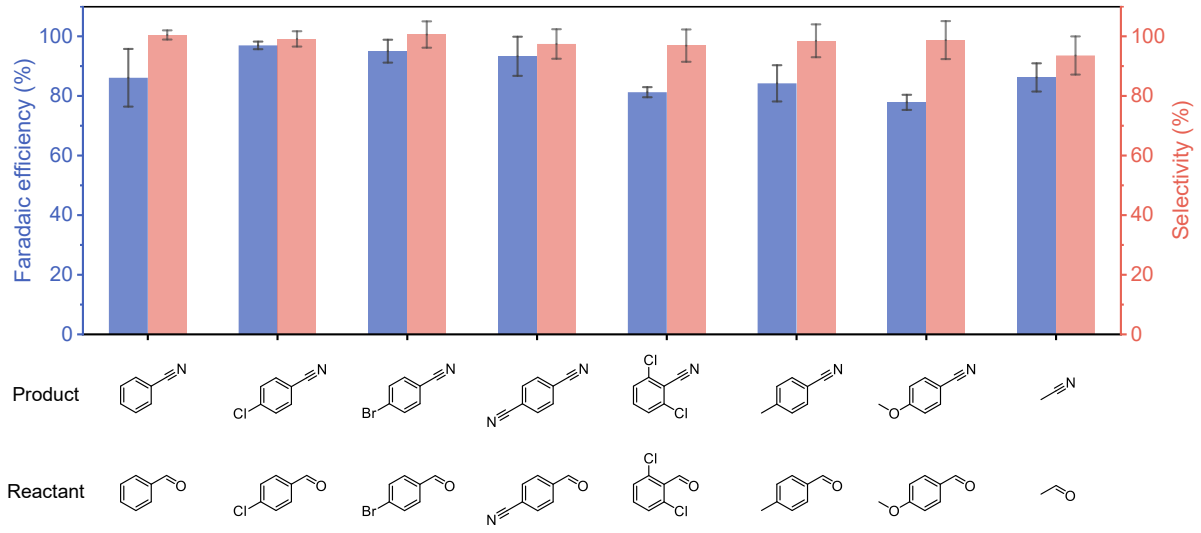

Supplementary Fig. 38 | Faradaic efficiencies and selectivities of the electrochemical conversion of aromatic and aliphatic aldehydes to the corresponding nitriles using the Co_3O_4/Cu_xO electrocatalyst at 1.35 V vs. RHE. All error bars represent standard deviation based on three independent samples. Source data for Supplementary Fig. 38 are provided as Source Data file.

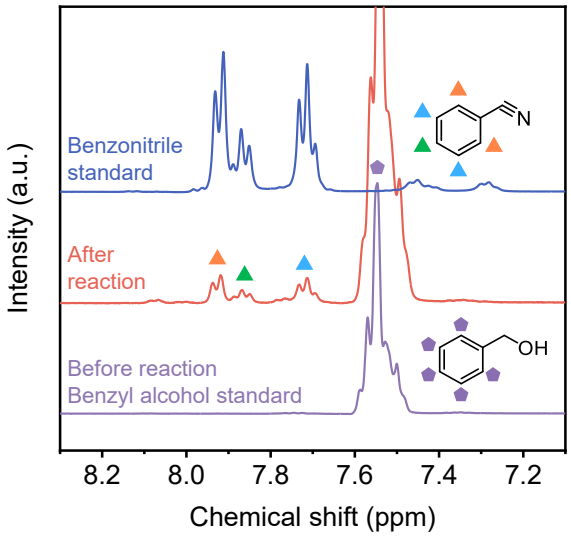

Supplementary Fig. 39 | ^{1}H NMR detection of the benzonitrile product after electrochemical benzyl alcohol-to-benzonitrile conversion using the Co_3O_4/Cu_xO electrocatalyst at 1.5 V vs. RHE. Source data for Supplementary Fig. 39 are provided as Source Data file.

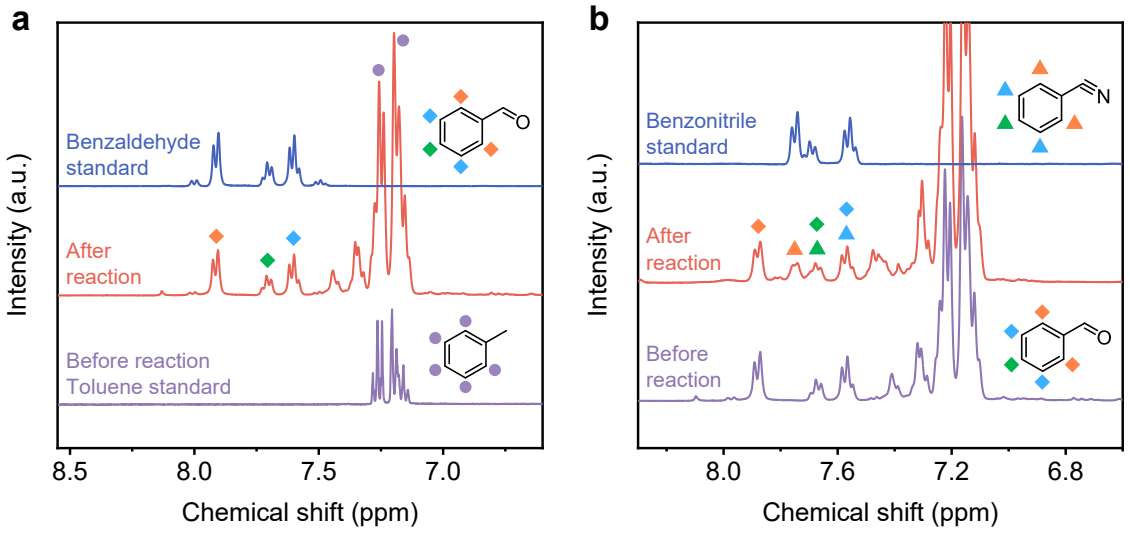

Supplementary Fig. 40 | Two-stage electrochemical toluene-to-benzonitrile conversion. a, ^{1}H NMR detection of the benzaldehyde intermediate after the electrochemical toluene-to-benzaldehyde conversion at 100 mA cm^{-2} current density using the CoO_x/IrO_2 on Ti mesh electrode. **b**, ^{1}H NMR detection of the benzonitrile product after the electrochemical benzaldehyde-to-benzonitrile conversion at 25 mA cm^{-2} current density using the Co_3O_4/Cu_xO electrocatalyst. Source data for Supplementary Fig. 40a and 40b are provided as Source Data file.

Note: The concentration of benzaldehyde obtained from the electrochemical conversion of toluene was 29.1(±2.4) mM, and the residual toluene concentration is 124.3(±3.2) mM. This suggests reduced mass transport of benzaldehyde to the catalyst surface, as well as competition from toluene for adsorption sites. Thus, the Faradaic efficiency is lower than that of the direct conversion from benzaldehyde to benzonitrile.

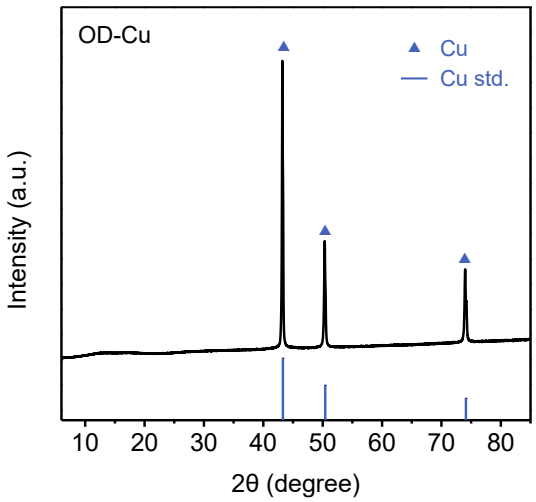

Supplementary Fig. 41 | XRD pattern of the oxide-derived Cu (OD-Cu) electrocatalyst for the cathodic nitrogen oxides reduction reaction (NO_xRR) to NH_3. Source data for Supplementary Fig. 41 are provided as Source Data file.

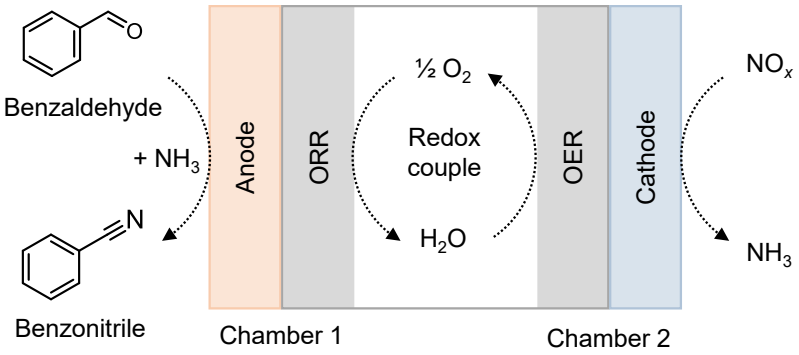

Supplementary Fig. 42 | Schematic of the tandem benzonitrile electrosynthesis and NO_xRR electrolyzer with decoupled configuration connected by O_2/H_2O redox couple.

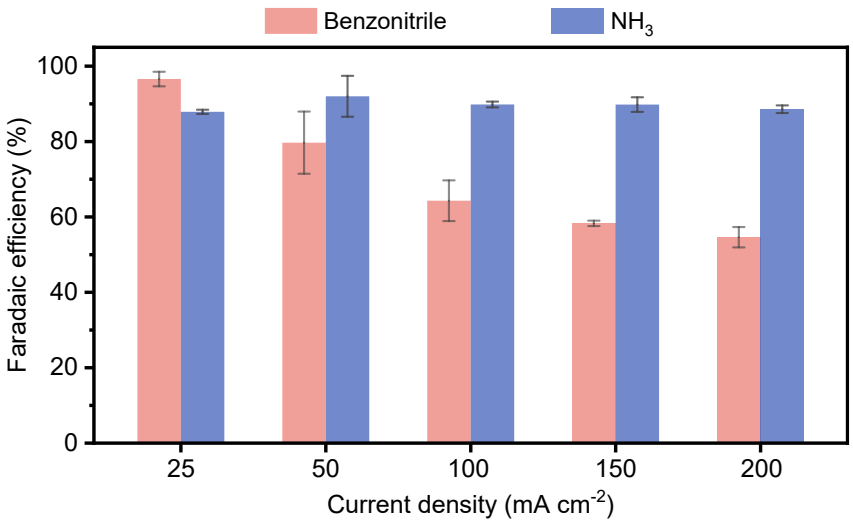

Supplementary Fig. 43 | Faradaic efficiencies towards benzonitrile and NH_3 in the tandem benzonitrile electrosynthesis and NO_xRR electrolyzer at different current densities. All error bars represent standard deviation based on three independent samples. Source data for Supplementary Fig. 43 are provided as Source Data file.

Supplementary Table 1 | *K*-point convergence test for phenylmethanimine adsorption on the $Cu_2O(111)$ surface, with and without the DFT+U correction (U = 5 eV)[1]. Geometries for Configurations 1 and 2 are illustrated in Supplementary Fig. 30.

Calculation setting	Adsorption configuration	Relative energy (eV)
1×1×1	Configuration 1	0.00
	Configuration 2	−0.10
1×1×1 + U	Configuration 1	0.00
	Configuration 2	−0.11
2×2×1	Configuration 1	0.00
	Configuration 2	−0.10
2×2×1 + U	Configuration 1	0.00
	Configuration 2	−0.10

Supplementary Table 2 | Gibbs free energy profile for the stepwise dehydrogenation of *Ph−CH=NH to *Ph−CH=N and *Ph−C≡N on CuO(111), Cu_2O(111) and Co_3O_4(311) surfaces. For each surface, the energy of *Ph–CH=NH is taken as the zero reference.

Surface	*Ph−CH=NH	*Ph−CH=N	*Ph−C≡N
CuO(111)	0.00	0.70	0.50
Cu_2O(111)	0.00	1.16	0.49
Co_3O_4(311)	0.00	0.96	0.53

Supplementary Table 3 | Bader charge analysis of *Ph−CH=NH, *Ph−CH=N, and *Ph−C≡N adsorbed on the CuO(111) surface.

Bader charge	*Ph−CH=NH	*Ph−CH=N	*Ph−C≡N
Molecule	+0.16	+0.85	+2.1
Surface	−0.16	−0.85	−2.1

Supplementary Table 4 | Comparison of current density (*j*), partial current density ($j_{\text{partial, benzonitrile}}$), Faradaic efficiency, selectivity and production rate of benzonitrile against that of previously-reported nitrile electrosynthesis.

Catalyst	Electrolyte	Cell type	j (mA cm^{-2})	$j_{\text{partial, benzonitrile}}$ (mA cm^{-2})	Faradaic efficiency (%)	Selectivity (%)	Production rate (mmol cm^{-2} h^{-1})	Reference
Co_3O_4/Cu_xO	1 M NaOH, 0.05 M benzaldehyde and 2 M NH_3	H-type cell	25	24.2	96.6	97.9	0.45	**This work**
			200	109.5	54.6	99.6	2.04	
ZnO/Sn/SnO_2	0.1 mmol phenylacetaldehyde, 0.5 mmol KNO_3 and 1 mmol cyanuric chloride	H-type cell	12	0.72	~6	79	~0.005	2
Ni foam	20 mM benzyl alcohol, 1 M NH_3, pH 13	H-type cell	~2.0	~1.0	49.4	~59.8	~0.009	3
Pb cathode	0.1 M benzoic acid, 0.2 M KI in liquid ammonia	A pressure-resistant electrochemical cell	25	8	32	~4.6	~0.005	4
Cu_1Pd_1	0.5 M K_2CO_3,10 mM benzyl alcohol, 1.5 M $NH_3 \cdot H_2O$	H-type cell	~17	~10.5	61.8	86.9	~0.098	5
Pd@CuO	0.1 M KOH, 10 mM benzyl alcohol and 2 M ammonia	H-type cell	~2.2	~1.1	~51	83.2	~0.010	6
NiCo-N/CC	1 M NaOH, 0.1 M benzyl alcohol and 4 M NH_4Cl	H-type cell	~7.2	~3.7	52	70.1	~0.035	7

References

1. Scanlon D. O., Morgan B. J., Watson G. W. Modeling the polaronic nature of *p*-type defects in Cu_2O: The failure of GGA and GGA+U. *J. Chem. Phys.* **131**, 124703 (2009).
2. Xue, C. et al. Electrosynthesis of Nitriles from Nitrate and Aldehyde via C≡N Bond Construction. *J. Am. Chem. Soc.* **147**, 32896–32903 (2025).
3. Xiao, Y., Lim, C. W., Gao, L. & Yan, N. Electrosynthesis of nitriles from primary alcohols and ammonia on Ni catalysts. *Green Chem.* **27**, 5715–5727 (2025).
4. Maeda, Y., Sakuragi, K. & Kawase, M. Direct cyanation reaction from benzoic acid to benzonitrile by paired electrosynthesis in liquid ammonia. *RSC Adv.* **15**, 17562–17569 (2025).
5. Sun, L. et al. Synergistic effect of Cu_1Pd_1 electrocatalyst with N/O asymmetric coordination for C-O bonds to C≡N bonds boosting hydrogen production. *Appl. Catal. B Environ.* **378**, 125580 (2025).
6. Fang, Z. et al. Synthesis of nitriles by the electro-oxidative coupling of primary alcohols and ammonia on Pd nanoparticle-modified CuO nanowires in oxidant-free electrolytes under ambient conditions. *Appl. Catal. B Environ.* **337**, 122999 (2023).
7. Mushiana, T., Shao, Z., Khan, M., Zhang, N. & Ma, M. Selective electrocatalytic conversion of primary alcohols to nitriles on nickel-cobalt nitride/oxide tandem electrocatalyst. *Chem. Eng. J.* **477**, 146742 (2023).